



CHALMERS
UNIVERSITY OF TECHNOLOGY

Mn-doped WSe₂ as an efficient electrocatalyst for hydrogen production and as anode material for lithium-ion batteries

Downloaded from: <https://research.chalmers.se>, 2026-05-20 01:04 UTC

Citation for the original published paper (version of record):

Kagkoura, A., Wei, S., Zeng, L. et al (2024). Mn-doped WSe₂ as an efficient electrocatalyst for hydrogen production and as anode material for lithium-ion batteries. *Nanoscale*, 17(2): 947-954. <http://dx.doi.org/10.1039/d4nr04348k>

N.B. When citing this work, cite the original published paper.



Cite this: *Nanoscale*, 2025, **17**, 947

Mn-doped WSe₂ as an efficient electrocatalyst for hydrogen production and as anode material for lithium-ion batteries†

Antonia Kagkoura,^{id} *^a Shuangying Wei,^{id} ^a Lunjie Zeng,^b Eva Olsson,^{id} ^b
 Filipa M. Oliveira,^{id} ^a Jan Luxa^a and Zdeněk Sofer^{id} *^a

The ongoing energy crisis has made it imperative to develop low-cost, easily fabricated, yet efficient materials. It is highly desirable for these nanomaterials to function effectively in multiple applications. Among transition metal dichalcogenides, tungsten diselenide (WSe₂) shows great promise but remains understudied. In this work, we doped WSe₂ with Mn using a simple hydrothermal method. The resulting material exhibited excellent electrocatalytic activity for the hydrogen evolution reaction, achieving a low overpotential of -0.28 V vs. RHE at -10 mA cm⁻², enhanced conductivity, and high stability and durability. Moreover, as an anode material in lithium-ion batteries, the Mn-doped WSe₂ outperformed pristine WSe₂, reaching initial discharge capacities of 1223 and 922 mA h g⁻¹, respectively. Additionally, the Mn-doped material maintained a significantly higher discharge capacity of 201 mA h g⁻¹ compared to intact WSe₂, which had 68 mA h g⁻¹ after 150 cycles. This work offers novel insights into designing efficient bifunctional nanomaterials using transition metal dichalcogenides.

Received 22nd October 2024,
 Accepted 4th November 2024

DOI: 10.1039/d4nr04348k

rsc.li/nanoscale

Introduction

The struggle to keep up with the ever-rising energy demand in the world has become one of humanity's most significant battles. With an increasing population, our hunger for anything that consumes a lot of energy continuously grows. This indicates that the reserves of conventional fossil fuels will dwindle over time, while renewable energy alternatives must take center stage. A major appeal for these alternatives is their environmentally friendly nature, low pollution footprint, and economic viability.¹ Hence, large-scale electrical energy storage technologies are in dire need of development.¹⁻³

Electrochemical water splitting is another promising green process for hydrogen production. However, high cost and availability of current platinum-based electrocatalysts remain bottlenecks to large-scale commercialization.^{4,5} Besides this, lithium-ion batteries (LIBs) are considered the ideal candidates for storing electrical energy in portable and electrical vehicles considering their lightweight frame, high energy density, compact size,

negligible memory effects, long cycle lifetime, and minimal environmental impact.⁶ Up until today, a major driving force for further improvement in capacity is finding an alternative to graphite as an active anode material.⁷⁻⁹ The specific capacity of graphite during discharging is inherently restricted to 372 mA h g⁻¹ and thus restricts the overall capacity of LIBs.¹⁰ Since the energy density for batteries is increasing day by day, the said limitation becomes highly crucial and hence demands the development of some alternative anode materials that shall provide higher capacity and improve the performance of next-generation energy storage systems.

Transition metal dichalcogenides (TMDs) have emerged as an attractive alternative in electrocatalysis, with particular emphasis on hydrogen evolution reaction (HER), based on their natural abundance and inexpensiveness.^{11,12} Consequently, bottom-up approaches based on hydrothermal or solvothermal reactions between metallic and chalcogen molecular precursors enable the synthesis of high yields of both polymorphs of TMDs.^{13,14} Abundant defects and exposed edges are generated by such an approach, which improves the electrocatalytic activity of the material for HER. More interestingly, the TMDs are strong candidates as anode materials for LIBs owing to their outstanding chemical stability, low cost and high theoretical capacities.^{15,16} Their big interlayer spacing also promotes the reversible lithium ion transport and insertion/extraction reaction process.^{15,16}

Among the TMDs members, WSe₂ has a layered structure with a large interlayer distance as high as 0.65 nm, enabling

^aDepartment of Inorganic Chemistry, Faculty of Chemical Technology, University of Chemistry and Technology Prague, Technická 5, 166 28 Prague 6, Czech Republic.

E-mail: kagkourn@vscht.cz, soferz@vscht.cz

^bDepartment of Physics, Chalmers University of Technology, 41296 Göteborg, Sweden

†Electronic supplementary information (ESI) available: XPS spectra for Mn-WSe₂, table for electrocatalytic HER parameters in for all tested materials and cyclic voltamographs of (a) Mn-WSe₂ and (b) WSe₂. See DOI: <https://doi.org/10.1039/d4nr04348k>



highly efficient lithium-ion diffusion. In addition, its density is as high as 9.32 g cm^{-3} ; hence, WSe_2 has great promise for high volumetric energy densities – a crucial parameter for demanding applications such as electric vehicles.^{17,18} However, nanostructured WSe_2 anodes are barely explored yet. In the case of electrocatalysis as well, WSe_2 has received less attention from the TMD family compared to molybdenum disulfide, although WSe_2 has presented very good activity in the HER.^{13,19} Till now, the electrocatalytic HER activity of TMDs has been improved by tuning several parameters such as phase engineering and heteroatom doping.^{20,21} Indeed, metallic TMDs of the 1T type have intrinsic reduced charge-transfer resistance compared to semiconducting varieties of 2H type, favorable in electrocatalysis.^{20,21} Most importantly, the introduction of heteroatoms into TMDs is one of the most powerful ways to enhance their electrocatalytic activity.^{22,23} Particularly, element doping causes crystal distortion, thereby enhancing electronic structure. Besides that, due to the doped elements, some new adsorption sites are created increasing the total available adsorption sites in number.²² Moreover, element incorporation into the host structure is able to significantly improve the intrinsic conductivity of the material by changing the chemical bond or the local lattice, which is rather vital in the performance of LIBs.²⁴ Manganese (Mn) is a non-precious and thus inexpensive metal that has also proved to be an efficient dopant in TMDs for HER.^{25,26} However, its potential in WSe_2 with respect to HER and LIB remains unexplored up to now. Simpler doping processes remain scarce, and the processes at lower temperatures are few.²² Furthermore, WSe_2 -based materials are not widely explored in LIBs,^{17,18} and manganese-doped WSe_2 remains to be studied.

In this work, we adopt a simple hydrothermal method to dope Mn into WSe_2 , resulting in Mn- WSe_2 . Its electrocatalytic activity for HER is investigated; accordingly, it exhibits a low overpotential of 298 mV at -10 mA cm^{-2} and a low charge transfer resistance of 46Ω with high stability and durability. In fact, the advantages of Mn doping were realized in the far higher performance of Mn- WSe_2 when used, to the best of our knowledge, for the first time as an anode in lithium-ion batteries. Compared to pure WSe_2 , Mn- WSe_2 exhibited much higher initial discharge and charge capacities. In addition, even after 150 cycles, Mn- WSe_2 maintained much higher capacities of 201 mA h g^{-1} compared to 68 mA h g^{-1} for undoped WSe_2 .

Experimental

General

Chemicals, reagents, and solvents were purchased from Sigma-Aldrich and used without further purification.

SEM

The morphology of analyzed materials was investigated using scanning electron microscopy (SEM) with a Tescan MAIA-3 Field Emission Gun Scanning Electron Microscope (FEG-SEM).

To conduct the measurements, the samples were placed on a carbon conductive tape. SEM measurements were carried out at 5 kV acceleration voltage.

TEM

A JEOL monochromated ARM200F transmission electron microscope (TEM) operated at 200 kV was used for scanning transmission electron microscopy (STEM) and STEM-EDS analysis. The TEM is equipped with a CEOS probe aberration corrector, a CEOS image aberration corrector and a double silicon drift detector (SDD) for EDS. High angle annular dark field (HAADF) STEM imaging was used to directly visualize atomic structure of the crystals. The beam convergence half-angle and collection inner half-angle are $\sim 27 \text{ mrad}$ and 55 mrad , respectively. The resolution for STEM imaging is $\sim 0.8 \text{ \AA}$. STEM-EDS was used to map spatial distribution of elements at the nanometer and atomic scales. TEM specimens were prepared by manually grinding bulk crystals in IPA for 15 min in a mortar. The resultant solution with nanocrystals was drop-casted on holey carbon coated Cu grid and dried in air.

XPS

High resolution X-ray photoelectron spectroscopy (XPS) was performed using an ESCAProbeP spectrometer (Omicron Nanotechnology Ltd, Germany) with a monochromatic aluminium X-ray radiation source (1486.7 eV). Wide-scan surveys of all elements were performed, with subsequent high-resolution scans of the C 1s and O 1s. Relative sensitivity factors were used to evaluate the carbon-to-oxygen (C/O) ratios from the survey spectra. The samples were placed on a conductive carrier made from a high purity silver bar. An electron gun was used to eliminate sample charging during measurement ($1\text{--}5 \text{ V}$). X-ray powder diffraction (XRD) data were collected at room temperature on Bruker D8 Discoverer (Bruker, Germany) powder diffractometer with parafocusing Bragg–Brentano geometry using $\text{CuK}\alpha$ radiation ($\lambda = 0.15418 \text{ nm}$, $U = 40 \text{ kV}$, $I = 40 \text{ mA}$). Data were scanned over the angular range $5\text{--}90^\circ$ (2θ) with a step size of 0.019° (2θ). Data evaluation was performed in the software package EVA.

Raman spectroscopy

InVia Raman microscope (Renishaw, England) in backscattering geometry with CCD detector was used for Raman spectroscopy. DPSS laser (532 nm , 50 mW) with applied power of 5 mW and $50\times$ magnification objective was used for the measurement. Instrument calibration was achieved with a silicon reference which gives a peak position at 520 cm^{-1} and a resolution of less than 1 cm^{-1} . The samples were suspended in deionized water (1 mg ml^{-1}) and ultrasonicated for 10 min. The suspension was deposited on a small piece of silicon wafer and dried.

Electrochemical measurements

The electrochemical characterization by means of cyclic linear sweep voltammetry (LSV) was performed using an Autolab



PGSTAT 204 (Metrohm, Switzerland). A standard three-compartment electrochemical cell was used equipped with an RDE with a glassy carbon disk (geometric surface area: 0.196 cm²) as a working electrode, graphite rod as a counter-electrode, and Hg/HgSO₄ (0.5 M K₂SO₄) as reference electrode. HER LSV measurements were performed in N₂-saturated aqueous 0.5 M H₂SO₄ solution at room temperature. For preparing the catalyst ink, catalytic powder (4.0 mg) was dissolved in a mixture (1 mL) of deionized water, isopropanol, and 5% Nafion (v/v/v = 4:1:0.02) followed by sonication for 30 min before use. The working electrode was polished with alumina suspension, washed with deionized water, and finally sonicated in double-distilled water before casting 8.5 μL aliquots of the electrocatalytic ink on the electrode's surface. Finally, electrochemical impedance spectroscopy (EIS) measurements were acquired from 105 to 10⁻¹ Hz with an AC amplitude of 0.01 V.

Battery assembly and electrochemical measurements

Electrode fabrication was performed inside an argon-filled glovebox (MBRAUN, Germany; O₂ and H₂O < 0.1 ppm). The electrode slurry was formulated by mixing the active material (WSe₂ and Mn-WSe₂), PVDF binder, and CB conducting agent in a weight ratio of 7:2:1 using NMP as the solvent. This mixture was thoroughly homogenized to form a uniform slurry. The slurry was then doctor-bladed onto a 7 μm-thick copper foil current collector and dried in a heat pad oven at 70 °C for 12 hours. After drying, the coated foil was cut into disks of 15 mm diameter, which served as the electrodes. The mass loadings of the WSe₂ and Mn-WSe₂ electrodes ranged from 1.5 to 2.2 mg cm⁻². Two-electrode lithium cells (CR2025 coin cells, MTI Corporation) were assembled in the glovebox. Each cell comprised an electrode disk, a metallic lithium foil as the counter electrode, and a glass microfiber separator (Whatman, Grade GF/D). The assembly process was completed by immersing the components in the previously mentioned electrolyte solution. The electrochemical cycling of the WSe₂ and Mn-WSe₂ electrodes was evaluated in the CR2025 coin cells across a voltage range of 0.001 V to 3.0 V vs. Li⁺/Li. 150 cycles were performed at a constant current rate of 0.3 C (1C = 314 mA g⁻¹). All galvanostatic cycling measurements were carried out at room temperature using a Neware battery testing system (BTX 7.6, Shenzhen, China).

Preparation of WSe₂

Tungsten hexacarbonyl (1 mmol) and selenium powder (2 mmol) were dissolved in 30 mL DMF and the resulting suspension was transferred into a 50 mL Teflon-lined stainless-steel autoclave reactor and heated at 200 °C for 13 h. After the autoclave was cooled to room temperature, the resulting suspension was centrifuged at 10 000 rpm with DMF (2 times), water (3 times) and methanol (3 times).

Preparation of Mn-WSe₂

Initially, a mixture comprising 50 mg of manganese acetate tetrahydrate and 36 mg of thiourea was prepared in 1 mL of water and allowed to stand overnight, resulting in the formation of

the Mn ion complex, Mn(thiourea)₄²⁺. Subsequently, this solution of the Mn thiourea complex was introduced into 50 mL of a stabilized WSe₂ colloid solution (with a concentration of 1 mg mL⁻¹ and containing 30 v/v% isopropanol/water with 50 mg of polyvinylpyrrolidone). The resulting dispersion was then transferred to a 100 mL vessel autoclave and subjected to hydrothermal treatment at 160 °C for 24 h.

Results and discussion

The synthesis of Mn-WSe₂ begins with a solvothermal reaction to produce WSe₂, and then the doping of Mn atoms is directly achieved by hydrothermal reaction. The process involves the preparation of the thiourea-manganese complex that targets the surface selenium vacant sites of WSe₂ and occupies them through the strong molecular affinity representative of defective sites.²⁷ Mn-WSe₂ was characterized using Raman spectroscopy and X-ray photoelectron spectroscopy (XPS), as depicted in Fig. 1 and 2, respectively. Notably, the spectrum of Mn-WSe₂ displays bands at 128, 202, and 236 cm⁻¹, corresponding to J₁, J₂, and J₃, which are indicative of the metallic 1T octahedral phase of WSe₂.²⁸ Additionally, bands at 256 cm⁻¹ for Mn-WSe₂ arise from the overlapping E_{12g} and A_{1g} modes, characteristic of the 2H-phase.²⁸ These same bands are shifted to higher wavenumbers by 4 cm⁻¹ compared to pristine WSe₂, indicating successful doping.²⁹

The 1T phase is confirmed by the deconvoluted W 4f spectrum of Mn-WSe₂, which shows a doublet of the W⁴⁺ peaks at 30.8 eV for W⁴⁺ 4f_{7/2} and 33.7 eV for W⁴⁺ 4f_{5/2}, assigned to the 1T phase (Fig. 2a).¹⁴ The shifts to lower binding energy compared to pristine WSe₂ (31.6 eV for W⁴⁺ 4f_{7/2} and 33.7 eV for W⁴⁺ 4f_{5/2}), as seen in (Fig. 2c), strongly indicate successful Mn doping.³⁰ Additionally, signals at 32.43 and 34.53 eV correspond to W⁴⁺ 4f_{7/2} and W⁴⁺ 4f_{5/2} of the 2H phase. Peaks at 34.9 and 37.8 eV are associated with the presence of W⁶⁺ species within WSe₂, favorable in electrocatalytic reactions.^{31–33} Moreover, the Se 3d peak profile of Mn-WSe₂ can be deconvoluted into two sets of doublet peaks: the higher energy peaks at

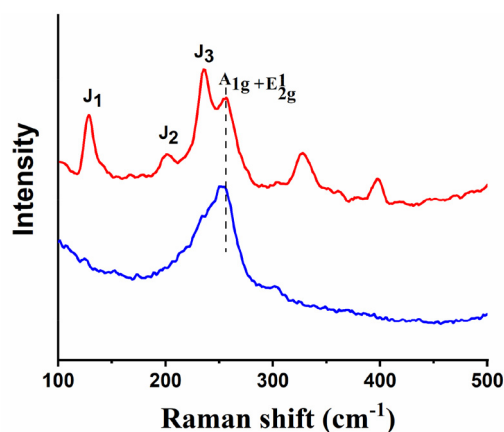


Fig. 1 Raman spectra (532 nm) for Mn-WSe₂ (red) and WSe₂ (blue).



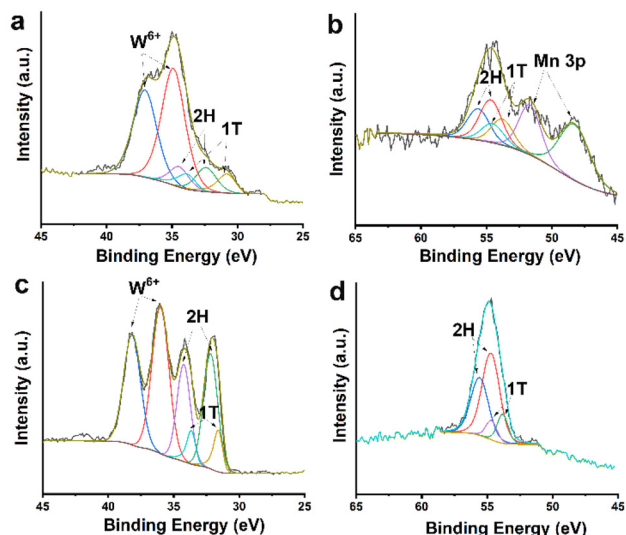


Fig. 2 Deconvoluted X-ray photoelectron spectra of (a) W 4f and (b) Se 3d for Mn-WSe_2 . (c) W 4f and (d) Se 3d for WSe_2 .

55.68 eV for Se $3d_{3/2}$ and 54.7 eV for Se $3d_{5/2}$ correspond to the 2H phase, while the lower energy peaks at 54.62 eV for Se $3d_{3/2}$ and 53.82 eV for Se $3d_{5/2}$ correspond to the 1T phase (Fig. 2b). Signals at higher energies are attributed to Mn 3p. For pristine WSe_2 , doublets for 2H and 1T phases, are located in higher energies, doublets at 55.61 eV for Se $3d_{3/2}$ and 54.74 eV for Se $3d_{5/2}$ (2H phase) and 54.78 eV for Se $3d_{3/2}$ and 53.86 eV for Se $3d_{5/2}$ (1T phase), as seen in Fig. 2d. All observed shifts support that Mn doping modifies the redox states of both W and Se.³⁰ Additionally, the Mn 2p spectrum displays two spin-orbit doublets: Mn $2p_{3/2}$ at 641.28 eV and Mn $2p_{1/2}$ at 653.5 eV, corresponding to Mn^{2+} (Fig. S1†).³⁴ Further evidence supporting the hybrid structure was obtained through powder X-ray diffraction (XRD). Fig. S2† shows the reflection signals corresponding to plane reflections of hexagonal WSe_2 (reference JCPDF no. 38-1388).³⁵

The morphological and elemental analysis of Mn-WSe_2 along with the intact WSe_2 was realized by scanning electron microscopy (SEM) and transmission electron microscopy (TEM). SEM images in Fig. 3 reveal that both pristine and doped WSe_2 nanostructures exhibit a similar morphology, with small, randomly oriented nanosheets interconnected to form intricate, flower-like formations. During the solvothermal process, these nanosheets self-assembled into larger, micro-scale “ball-flowers” with a hierarchical structure—indicating an organization that extends from the nanoscale sheets to complex, micro-scale formations. This morphology is common for TMDs deriving from solvothermal bottom-up approaches.^{13,14}

High-angle annular dark field (HAADF) scanning transmission electron microscopy (STEM) imaging shows the microscopic structure of the doped and pristine WSe_2 at the nanometer and atomic scales (Fig. 4). STEM images clearly show that WSe_2 nanocrystals (Fig. 4a and c) consist of randomly dis-

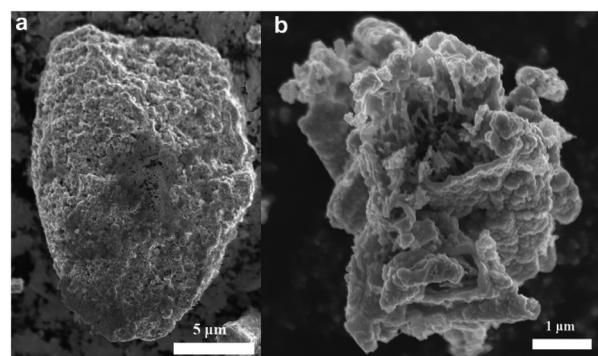


Fig. 3 SEM images of (a) Mn-WSe_2 and (b) pristine WSe_2 .

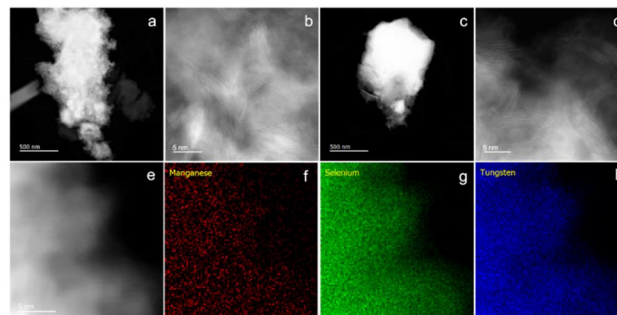


Fig. 4 (a) and (b) HAADF STEM images of Mn-WSe_2 . (c) and (d) HAADF STEM images of pristine WSe_2 . (e)–(h) HAADF STEM image and the corresponding STEM-EDXS elemental maps of Mn, Se and W.

tributed WSe_2 nanosheets (Fig. 4b and d). In the STEM images of both doped and pristine WSe_2 , there are fringes with an inter-fringe distance of ~ 0.65 nm (Fig. 4b and d), which is the interlayer distance in WSe_2 . The fringes are from nanoscale WSe_2 sheets, which are randomly orientated and distributed within the crystals. When the basal atomic planes in the nanosheets are parallel to the electron beam direction, fringes that show the stacking of basal planes are visible. The thickness of the WSe_2 nanosheets is about 5 nm and the length of the nanosheets is usually larger than 10 nm. Furthermore, the elemental distribution of Mn in Mn-WSe_2 was analyzed by STEM-energy dispersive spectroscopy (EDS) mapping. STEM-EDS maps and the corresponding STEM image of a doped WSe_2 nanocrystal are shown in Fig. 4e–h. As evident from the elemental maps, Mn is homogeneously and randomly distributed within the WSe_2 matrix at the nanometer and atomic scales. On average, the atomic concentration of Mn is $\sim 4\%$.

The electrocatalytic performance of Mn-WSe_2 in the HER was assessed using linear sweep voltammetry (LSV) in an aqueous 0.5 M H_2SO_4 electrolyte (Fig. 5a). Interestingly, Mn-WSe_2 showed a low onset potential at -0.077 V vs. RHE, only slightly lower-by 71 mV – of that of Pt/C at -0.006 V versus RHE; onset potentials were recorded at $j = -1$ mA cm^{-2} for all materials.³⁶ By contrast, pristine WSe_2 showed a much higher



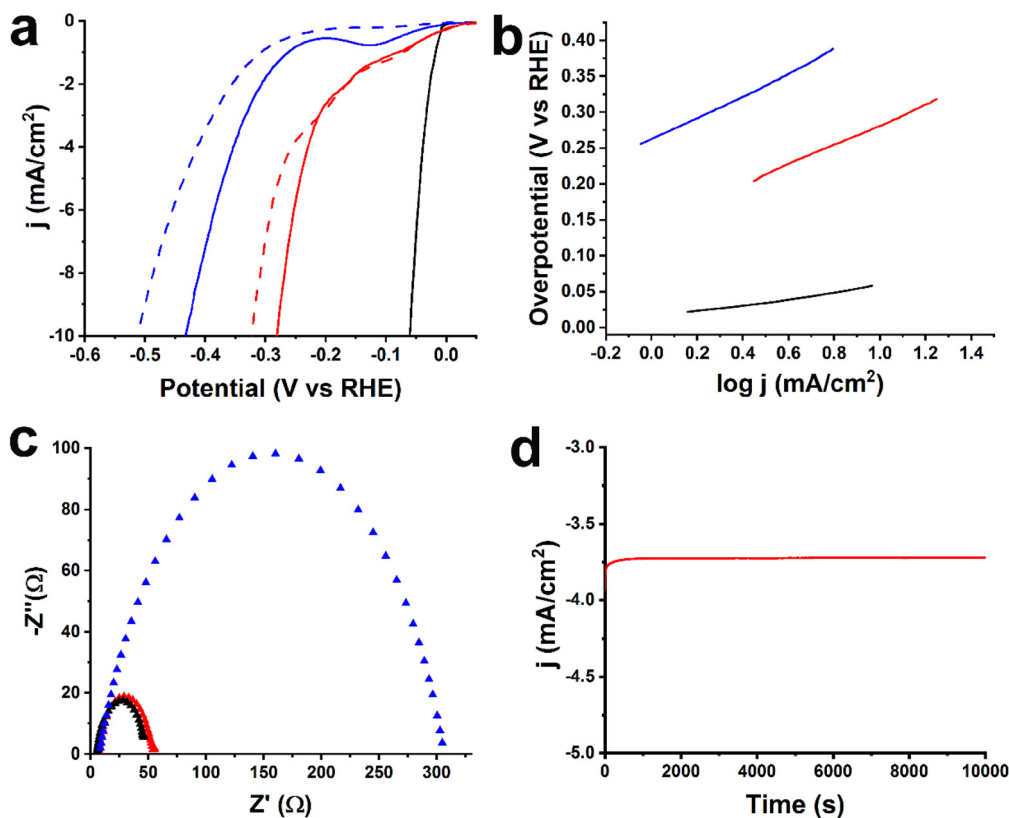


Fig. 5 (a) LSVs for HER obtained at 1600 rpm rotation speed and 5 mV s^{-1} scan rate before (solid lines) and after 10 000 cycles (dashed lines) in aqueous $0.5 \text{ M H}_2\text{SO}_4$, (b) Tafel slopes, (c) Nyquist plots for Mn-WSe₂ (red), WSe₂ (blue) and Pt/C (black) and (d) chronoamperometric response at -2.16 V (versus RHE) for 10 000 s for Mn-WSe₂.

onset overpotential of 193 mV than Mn-WSe₂ at -0.27 V vs. RHE. Moreover, the electrocatalytic activity of HER was further determined at the current density of -10 mA cm^{-2} . Interestingly, Mn-WSe₂ exhibited an overpotential as low as 280 mV, 150 mV lower than that of pristine WSe₂. Such improvement in catalytic performance arises from the preserved coordination vacancies due to the confined atoms acting as active catalytic sites. Strong electronic interaction between the incorporated Mn heteroatoms and WSe₂ induces new electronic states that are favorable for electrocatalytic activity.

To investigate the mechanism of the reaction, Tafel slopes were obtained from LSV curves. Mn-WSe₂ presented a smallest Tafel slope of 80 mV dec^{-1} in expectation, which means that the rate-determining reaction step is the desorption of absorbed hydrogen atoms from the electrode (Heyrovsky step). In sharp contrast, the pristine WSe₂ showed a much higher Tafel slope value of 143 mV dec^{-1} , which means that the rate-determining step corresponds to the initial proton adsorption onto the electrode surface through a reduction process (Volmer step). The easier reaction kinetics in the doped material can also be further evident from the EIS results depicted in Fig. 5c. Meanwhile, it also had a semicircle similar to Pt/C, which corresponded to the charge transfer resistance (R_{ct}) at 46Ω or close to that of Pt/C (42Ω). Meanwhile, the R_{ct}

value for pure WSe₂ was determined at around 299Ω , much higher than that of Mn-WSe₂, again underlining the positive effect of doping. The lower Tafel slope and R_{ct} values obtained in the doped material attested to higher conductance and more facile electron transfer kinetics and were ascribed to the successful incorporation of Mn atoms into the selenium defective sites.

Moving on, the stability of both doped and undoped WSe₂ was scrutinized by 10 000 consecutive electrocatalytic cycles, as described in Fig. 5a. Indeed, Mn-WSe₂ manifested a negligible potential loss of 40 mV, while WSe₂ revealed an overpotential as high as 80 mV. Additionally, chronoamperometric analysis was also conducted at a constant applied potential of -2.16 V vs. RHE for 10 000 s, accompanied by a rotation speed of 1600 rpm (Fig. 5d), in further evaluation of the durability of Mn-WSe₂. Astonishingly, Mn-WSe₂ showed excellent stability, reflecting only a negligible decay in current density of about 9%.

The electrochemically active surface area (ECSA) determination could deliver information about Mn-WSe₂ charge transport dynamics. ECSA values were calculated by using the equation $\text{ECSA} = C_{\text{dl}}/C_s$, wherein C_{dl} is the electrochemical double-layer capacitance and C_s is the specific capacitance of a flat surface taken as $40 \mu\text{F cm}^{-2}$ for the flat electrode having 1 cm^2 of real surface area. The cyclic voltammograms of Mn-



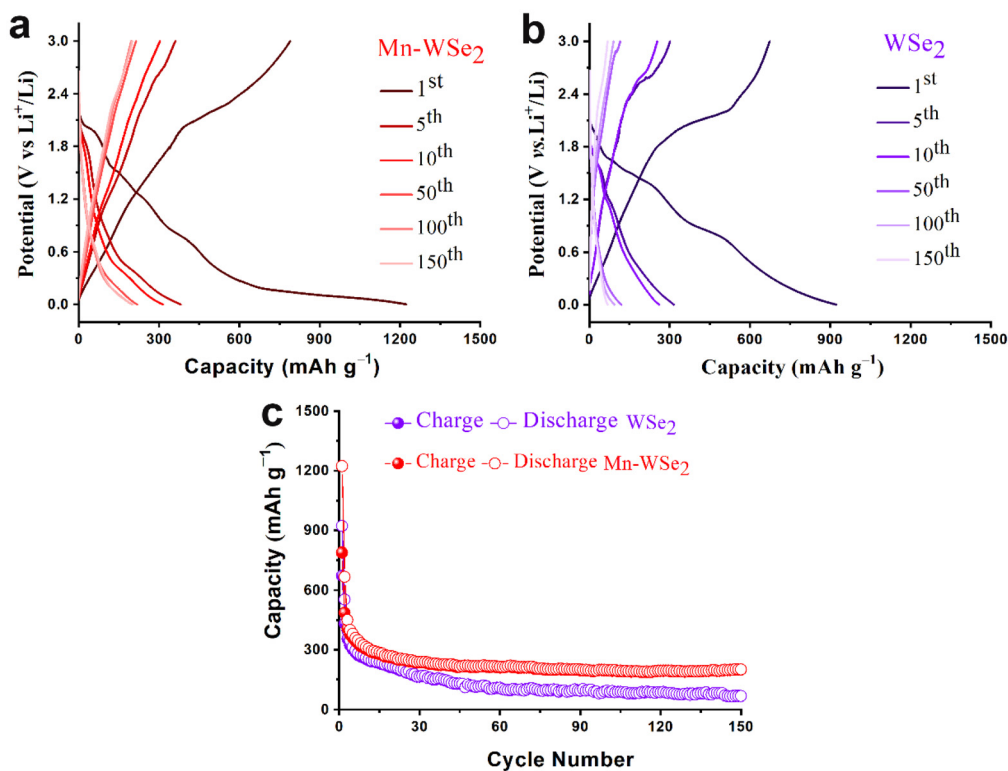


Fig. 6 Electrochemical evaluation of Mn-WSe₂ and WSe₂ electrodes in the lithium coin cells. Cycling performance of (a) Mn-WSe₂ and (b) WSe₂ in lithium coin cells galvanostatically cycled at a current rate of 0.3 C in terms of voltage profiles and (c) specific capacity vs. cycle number.

WSe₂ and pristine WSe₂ were recorded in a non-faradaic region at various scan rates ranging from 50 to 500 mV s⁻¹, as shown in Fig. S3 of the ESI.† Hence, Mn-WSe₂ gave the maximum ECSA value of about 21.95 cm² compared to an equivalent value of about 1.85 cm² for WSe₂. Values of ECSA are generally higher, pointing to a larger functional surface area of catalytic active sites and enabling improved electrocatalytic performance. Such results are also in good agreement with the overall electrocatalytic results. The summary of detailed electrocatalytic HER parameters for Mn-WSe₂ and other tested materials can be seen in Table S1.†

Next, the lithium storage capacities of Mn-WSe₂ and WSe₂ were evaluated using galvanostatic cycling measurements within a potential range of 0.001–3.0 V vs. Li⁺/Li. Fig. 6a and b illustrate the galvanostatic charge/discharge potential profiles for the Mn-WSe₂ and WSe₂ electrodes, respectively, which were recorded at a current density of 0.3 C (where 1C equals 314 mA g⁻¹). The initial discharge and charge profiles of the WSe₂ and Mn-WSe₂ electrodes reveal few discernible kinks or plateaus. Interestingly, the Mn-WSe₂ electrode exhibits a significantly higher initial discharge capacity of 1223 mA h g⁻¹ compared to 922 mA h g⁻¹ for pristine WSe₂. It also shows a higher charge capacity, with Mn-WSe₂ achieving 789 mA h g⁻¹ versus 673 mA h g⁻¹ for undoped WSe₂. These capacities are partially offset by the irreversible conversion process between WSe₂ and lithium ions (Li⁺), as well as the formation of a solid-electrolyte interface (SEI) film during the first cycle. Interestingly,

Mn-WSe₂ exhibits higher charge and discharge capacities compared to other WSe₂-based materials. For instance, WSe₂ grown onto graphene has demonstrated charge and discharge capacities of 531 and 744 mA h g⁻¹, respectively.¹⁸ Consequently, the initial coulombic efficiencies for Mn-WSe₂ and intact WSe₂ are 73.0% and 64.5%, respectively. Additionally, the subsequent cycles display consistent behavior, demonstrating the reversibility of the lithium storage reactions within Mn-WSe₂. Remarkably, the electrochemical performance of Mn-WSe₂ (200 mA h g⁻¹ after 100 cycles) surpasses that of previously reported WSe₂-based materials, such as few-layer thick WSe₂ nanosheets in 1T' crystal structures have shown a capacity of only 102 mA h g⁻¹ at 0.2 C after 100 cycles.¹⁷ Fig. 6c showcases the cycling stability over 150 cycles. The capacities maintain levels above 68 mA h g⁻¹ for WSe₂ and 201 mA h g⁻¹ for Mn-WSe₂ through the 150th cycle. The improved cycling performance of Mn-WSe₂ can be attributed to the successful incorporation of Mn, which significantly enhances the material's conductivity and greatly promotes charge transfer during the electrochemical reaction.

Conclusions

In summary, Mn-WSe₂ was synthesized *via* a simple hydrothermal method in which Mn atoms were introduced into flower-like nanostructured WSe₂. The confined Mn atoms



retained coordination vacancies and hence could provide catalytically active sites. As a result, Mn-WSe₂ exhibited excellent electrocatalytic performance toward the HER, with the overpotential at -10 mA cm^{-2} reaching 280 mV. The strong electronic interaction between the incorporated heteroatoms and WSe₂ induces novel electronic states that bring a significant boost in performance due to improved charge transfer and accelerated reaction kinetics. Besides, Mn-WSe₂ exhibits excellent stability, with only a slight increase in overpotential after 10 000 cycles and negligible loss of current density after 10 000 seconds. The beneficial role of Mn atoms was also reflected in the performance of Mn-WSe₂ as an anode material for lithium-ion batteries. Indeed, Mn-WSe₂ showed much larger initial discharge and charge capacities compared to pristine WSe₂. Additionally, Mn-WSe₂ maintained remarkably higher discharge capacities after 150 cycles, reaching 201 mA h g⁻¹ compared to 68 mA h g⁻¹ for bare WSe₂. Accordingly, it is highly desirable to develop easily fabricated yet efficient nanomaterials for a variety of energy-related applications. The above results illustrated that Mn-WSe₂ can act as an outstanding candidate for energy storage applications.

Data availability

The datasets generated during and/or analyzed during the study are accessible via the Zenodo repository: <https://zenodo.org/records/13789692>.

Conflicts of interest

There are no conflicts to declare.

Acknowledgements

The research leading to these results was supported by the Johannes Amos Comenius Programme, European Structural and Investment Funds, project 'CHEMFELLS VI' (No. CZ.02.01.01/00/22_010/0008122) from the Ministry of Education, Youth and Sports (MEYS). Financial support from Swedish Research Council (VR) and Swedish Foundation for Strategic Research (SSF) for the access to ARTEMI, the Swedish National Infrastructure in Advanced Electron Microscopy (2021-00171 and RIF21-0026) is also acknowledged. This work was performed in part at the Chalmers Material Analysis Laboratory, CMAL. Shuangying Wei gratefully acknowledges the financial support from the University of Chemistry and Technology Prague through the Rector's Junior Grant No. 101852403. This work was supported by the project "The Energy Conversion and Storage" funded as project No. CZ.02.01.01/00/22_008/0004617 by Programme Johannes Amos Comenius, call Excellent Research.

References

- 1 S. Z. S. Al Ghafri, S. Munro, U. Cardella, T. Funke, W. Notardonato, J. P. M. Trusler, J. Leachman, R. Span, S. Kamiya, G. Pearce, A. Swanger, E. D. Rodriguez, P. Bajada, F. Jiao, K. Peng, A. Siahvashi, M. L. Johns, L. Michael and E. F. May, *Energy Environ. Sci.*, 2022, **15**, 2690–2731.
- 2 I. Staffell, D. Scamman, A. V. Abad, P. Balcombe, P. E. Dodds, E. Paul, N. Shah and K. R. Ward, *Energy Environ. Sci.*, 2019, **12**, 463–491.
- 3 X. Wei, C.-C. Lin, C. Wu, N. Qaiser, Y. Cai, A. Y. Lu, K. Qi, J.-H. Fu, Y.-H. Chiang, Z. Yang, L. Ding, O. S. Ali, W. Xu, W. Zhang, M. B. Hassine, J. Kong, H. Y. Chen and V. Tung, *Nat. Commun.*, 2022, **13**, 6006.
- 4 K. H. Modi, P. M. Pataniya and C. K. Sumesh, *Chem. – Eur. J.*, 2024, **30**, e202303978.
- 5 S. Lee, S. Lee, C. Kim and Y.-K. Han, *Mater. Today Energy*, 2024, **43**, 101581.
- 6 P. U. Nzereogu, A. D. Omah, F. I. Ezema, E. I. Iwuoha and A. C. Nwanya, *Appl. Surf. Sci. Adv.*, 2022, **9**, 100233.
- 7 H. Hossain, M. A. Chowdhury, N. Hossain, A. Islam and M. H. Mobarak, *Chem. Eng. J. Adv.*, 2023, **16**, 100569.
- 8 Z. Shi, H. Huang, C. Wang, M. Huo, S.-H. Ho and H.-S. Tsai, *J. Chem. Eng.*, 2022, **447**, 137469.
- 9 X. Yu, Y. Ding and J. Sun, *iScience*, 2023, **26**, 107489.
- 10 Z. Zhao and H. N. Alshareef, *Adv. Mater.*, 2024, **36**, 2309223.
- 11 Y. Jia, Y. Zhang, H. Xu, J. Li, M. Gao and X. Yang, *ACS Catal.*, 2024, **14**, 4601–4637.
- 12 A. Raza, J. Z. Hassan, U. Qumar, A. Zaheer, Z. U. D. Babar, V. Iannotti and A. Cassinese, *Mater. Today Adv.*, 2024, **22**, 100488.
- 13 Z. Sun, Y. Wang, J. Lang, M. Yang, F. Jin and Y. H. Hu, *J. Mater. Chem. A*, 2021, **9**, 13490–13495.
- 14 A. Kagkoura, C. Stangel, R. Arenal and N. Tagmatarchis, *J. Phys. Chem. C*, 2022, **126**, 14850–14858.
- 15 F. Chen, S. J. Robertson, X. Xu, S. Chen, C. Sun, M. Shao and J. Wang, *Nano Energy*, 2024, **123**, 109414.
- 16 C. J. Price, E. A. D. Baker and S. P. Hepplestone, *J. Phys. Chem. C*, 2024, **128**, 1867–1876.
- 17 P. Zhou, G. Collins, Z. Hens, K. M. Ryan, H. Geaney and S. Singh, *Nanoscale*, 2020, **12**, 22307–22316.
- 18 X. Wang, J. He, B. Zheng, W. Zhang and Y. Chen, *Electrochim. Acta*, 2018, **283**, 1660–1667.
- 19 A. Kagkoura, C. Stangel, R. Arenal and N. Tagmatarchis, *Nanomaterials*, 2023, **13**, 35.
- 20 C. Yue, F. Sun, N. Liu, Y. Liu, W. Bao, X. Zhang, C. Zhang, S. Ma, Y. Zhou, C. Feng and Y. Lu, *Fuel*, 2024, **357**, 129668.
- 21 A. Han, X. Zhou, X. Wang, S. Liu, O. Xiong, O. Zhang, L. Gu, Z. Zhuang, W. Zhang, F. Li, D. Wang, L.-J. Li and Y. Li, *Nat. Commun.*, 2021, **12**, 709.
- 22 Z. Liu, T. He, Q. Jiang, W. Wang and J. Tang, *Int. J. Hydrogen Energy*, 2022, **47**, 29698–29729.



- 23 Y. Ren, X. Miao, J. Zhang, Q. Lu, Y. Chen, H. Fan, F. Teng, H. Zhai, X. He, Y. Long, C. Zhang and P. Hu, *J. Mater. Chem. A*, 2023, **11**, 2690–2697.
- 24 H. Lim, S. Yu, W. Choi and S. O. Kim, *ACS Nano*, 2021, **15**, 7409–7420.
- 25 V. Kuraganti, A. Jain, R. Bar-Ziv, A. Ramasubramaniam and M. Bar-Sadan, *ACS Appl. Mater. Interfaces*, 2019, **11**, 25155–25162.
- 26 D. K. Perivoliotis, C. Stangel, Y. Sato, K. Suenaga and N. Tagmatarchis, *Small*, 2022, **18**, 2203032.
- 27 G. Liu, A. W. Robertson, A. Li, M. M.-J. Li, W. C. H. Kuo, M. T. Dardy, M. H. Muhieddine, Y. C. Lin, K. Suenaga, M. Stamatakis, J. H. Warner and S. C. E. Tsang, *Nat. Chem.*, 2017, **9**, 810–816.
- 28 Y. J. Park, H.-S. So, H. Hwang, D.-S. Jeong, H.-J. Lee, J. Lim, C.-J. Kim and H.-S. Shin, *ACS Nano*, 2022, **16**, 11059–11065.
- 29 X. Wen, W. Feng, X. Li, J. Yang, R. Du, P. Wang, H. Li, L. Song, Y. Wang, M. Cheng, J. He and J. Shi, *Adv. Mater.*, 2023, **35**, 2211690.
- 30 K. Wang, H. Zhou, L. Cheng, D. Li, Z. Hu, S. Chen, C. Wu, L. Song and B. Ge, *Inorg. Chem.*, 2023, **62**, 21257–21264.
- 31 J. Yang, Y. Cao, S. Zhang, Q. Shi, S. Chen, S. Zhu, Y. Li and J. Huang, *Small*, 2023, **19**, 2207295.
- 32 M. B. Costa, M. A. de Araújo, M. V. de Lima Tinoco, J. F. de Brito and L. H. Mascaro, *J. Energy Chem.*, 2022, **73**, 88–113.
- 33 J. Wei, J. Wang, W. Guo, H. Tang and J. Li, *J. Chem. Eng.*, 2023, **460**, 141783.
- 34 D. Sahoo, S. Tyagi, S. Agarwal, J. Shakya, N. Ali, W.-J. Yoo and B. Kaviraj, *Langmuir*, 2023, **39**, 7109–7121.
- 35 P. Martínez-Merino, E. Sani, L. Mercatelli, R. Alcántara and J. Navas, *ACS Sustainable Chem. Eng.*, 2020, **8**, 1627–1636.
- 36 X. Zou and Y. Zhang, *Chem. Soc. Rev.*, 2015, **44**, 5148–5180.

